Chapter 4

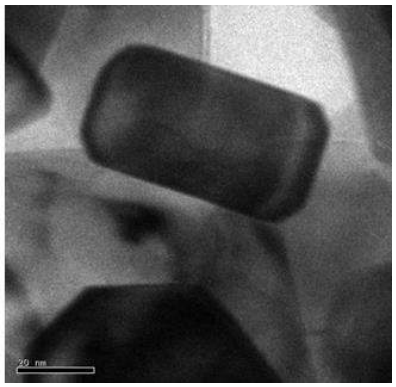

SYNTHESIS AND CHARACTERIZATION OF (Al_3Zr+ZrB_2)/Al-Mg *insitu* COMPOSITES

4.1 Introduction

There was limited improvement in the strength parameters of AA5052 Al-Mg alloy with incorporation of Al_3Zr particles, but the wear resistance was good enough as attributed by the larger size of particles. Here in the present investigation, the strength parameters of the Al_3Zr/Al-Mg composite are improved by the incorporation of smaller ZrB_2 particles. This chapter deals with the synthesis of hybrid (Al_3Zr+ZrB_2)/Al-Mg composites by direct melt reaction technique. Hybrid composites with different vol.% of ZrB_2 particles were prepared while keeping the amount of Al_3Zr particles fixed at 10 vol.%. The effect of different vol.% of ZrB_2 particles on the morphology, mechanical and tribological properties of Al_3Zr/Al-Mg composite has been presented.

4.2 Fabrication of Hybrid Composite

To prepare hybrid (Al_3Zr+ZrB_2)/Al-Mg composites with different vol.% of ZrB_2 particles, Al-Mg alloy (Al-2.26 wt.% Mg 0.13 wt.% Si, 0.30 wt.% Fe, 0.01 wt.% Cu, 0.10 wt.% Mn, 0.18 wt.% Cr), and two inorganic salts namely potassium-hexa-fluro-

zirconate (K_2ZrF_6) and potassium-tetra-fluro-borate (KBF_4) obtained from Sigma Aldrich Chemicals Pvt. Ltd, were taken as raw materials.

These composites were synthesized by DMR technique (cf; section 2.2). The required amount of inorganic powders was calculated according to stoichiometric reaction [Li et al., 2007, 2009] as mentioned in the Table 4.1 and Table 3.1 (cf; chapter 3). The quantity of powders corresponding to the vol.% of particles are given in Table 4.2 [Gautam and Mohan, 2015].

Table 4.1 – The calculation of theoretical volume fraction (%) of ZrB_2 particles in the composites.

Parameters	**Reactant**			**Product**
	10 Al	**3 K_2ZrF_6**	**6 KBF_4**	**3 ZrB_2**
Molecular weight	270	849	756	339
Density (g/cc)	2.68			6.09
Amount of reactant and product (g)	If the amount of alloy added is w and x is the presumed amount of Al to react	(849x/270)w = 3.144xw	(756x/270)w = 2.800xw	(339x/270)w = 1.256xw
Theoretical volume fraction	w/2.7			0.553x

Table 4.2 – The required quantity of powders for 500 g Al-Mg alloy in the composites [Gautam and Mohan, 2015].

Composites	**Quantity of powders ($x10^{-3}$ Kg)**	
	K_2ZrF_6	**KBF_4**
10 vol.% Al_3Zr	125.81	0
10 vol.% Al_3Zr + 1 vol.% ZrB_2	154.23	25.32
10 vol.% Al_3Zr + 3 vol.% ZrB_2	211.09	75.94
10 vol.% Al_3Zr + 5 vol.% ZrB_2	267.94	126.58

Temperature of Al alloy melt was raised to 885°C, inorganic salts dehydrated at 250°C for 3 hours were added to the melt, and mechanical stirring was applied. Four

compositions were prepared in which theoretical vol.% of Al_3Zr was kept constant (10 vol.%) and ZrB_2 vol.% was varied from 0 to 5. The composites are designated as C1, C2, C3 and C4 (Table 4.3). To obtain the actual vol.% of Al_3Zr and ZrB_2 particles in the four compositions, optical emission spectrometer study was carried out, and the chemical composition is shown in Table 4.4. Table 4.5 shows theoretical and actual vol.% of Al_3Zr and ZrB_2 particles in composites.

Table 4.3 – Composites and their designation [Gautam and Mohan, 2015].

Composite compositions	**Composites designation**
10 vol.% Al_3Zr	C1
10 vol.% Al_3Zr + 1 vol.% ZrB_2	C2
10 vol.% Al_3Zr + 3 vol.% ZrB_2	C3
10 vol.% Al_3Zr + 5 vol.% ZrB_2	C4

Table 4.4 – Chemical compositions of composites [Gautam and Mohan, 2015].

Element	**Si**	**Fe**	**Cu**	**Mn**	**Mg**	**Cr**	**Zn**	**Zr**	**B**	**Al**
C1	0.11	0.32	0.04	0.08	2.24	0.16	0.06	19.75	-	Bal.
C2	0.12	0.34	0.02	0.10	2.18	0.14	0.04	21.19	0.39	Bal.
C3	0.10	0.32	0.01	0.12	2.16	0.16	0.05	24.03	1.14	Bal.
C4	0.12	0.3	0.03	0.08	2.17	0.14	0.04	27.12	1.86	Bal.

Table 4.5 – Theoretical and actual vol.% of Al_3Zr and ZrB_2 particles in composites [Gautam and Mohan, 2015].

Composites	**Vol.% of reinforcements particles**			
	Theoretical		**Actual**	
	Al_3Zr	**ZrB_2**	**Al_3Zr**	**ZrB_2**
C1	10	0	9.07	0
C2	10	1	8.99	0.92
C3	10	3	8.90	2.68
C4	10	5	8.84	4.38

4.3 XRD Analysis

The XRD patterns of Al-Mg alloy and (Al_3Zr+ZrB_2)/Al-Mg hybrid composites with different amount of ZrB_2 particles are shown in Fig. 4.1. The analysis of diffraction peaks in the XRD pattern indicates the presence of Al, Al_3Zr and ZrB_2 phases. It is also observed from Fig. 4.1 that the intensity of ZrB_2 peaks increases with increasing vol.% of ZrB_2 particles. Possible chemical reactions between aluminium alloy and inorganic salts to form Al_3Zr intermetallic particles [Kumar et al., 2013] and for ZrB_2 particles [Tian et al., 2014] are given in eqns. (4.1) & (4.2) respectively [Gautam and Mohan, 2015].

$$3K_2ZrF_6 + 13Al \rightarrow 3Al_3Zr + 4AlF_{3(g)} + 6KF_{(g)} \quad (4.1)$$

$$3K_2ZrF_6 + 6KBF_4 + 10Al \rightarrow 3ZrB_2 + 9KAlF_{4(g)} + K_3AlF_{6(g)} \quad (4.2)$$

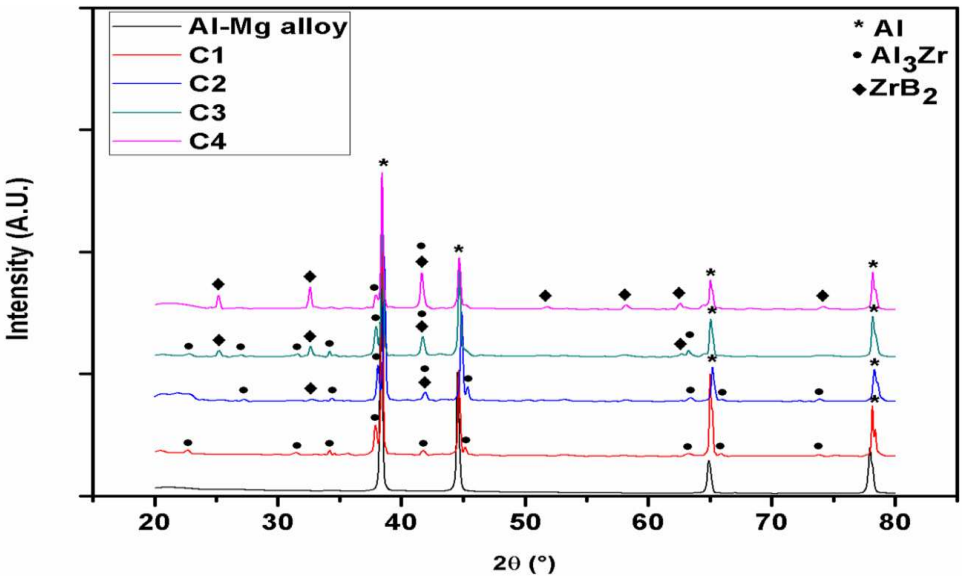

Figure 4.1 – XRD pattern of Al-Mg alloy and composites [Gautam and Mohan, 2015].

During generation of reinforcement particles, inorganic compounds such as $KAlF_4$, K_3AlF_6, AlF_3, and KF, are also formed as seen in above chemical reactions. These inorganic compounds are in gaseous form and exit from the molten alloy melt.

Therefore, residue of molten alloy melt consists only ZrB_2 and Al_3Zr particles in the Al-Mg alloy matrix. These reinforcement particles have also been confirmed by the extraction method. In this method, as cast hybrid composite is immersed in the 10% of hydrochloric acid solution for several days to completely dissolve the matrix and the reinforcement particles are filtered out. The extracted residue was analysed by XRD (Fig. 4.2) for different phases present. It shows only Al_3Zr and ZrB_2 peaks which confirms the successful formation of second phase reinforcement particles.

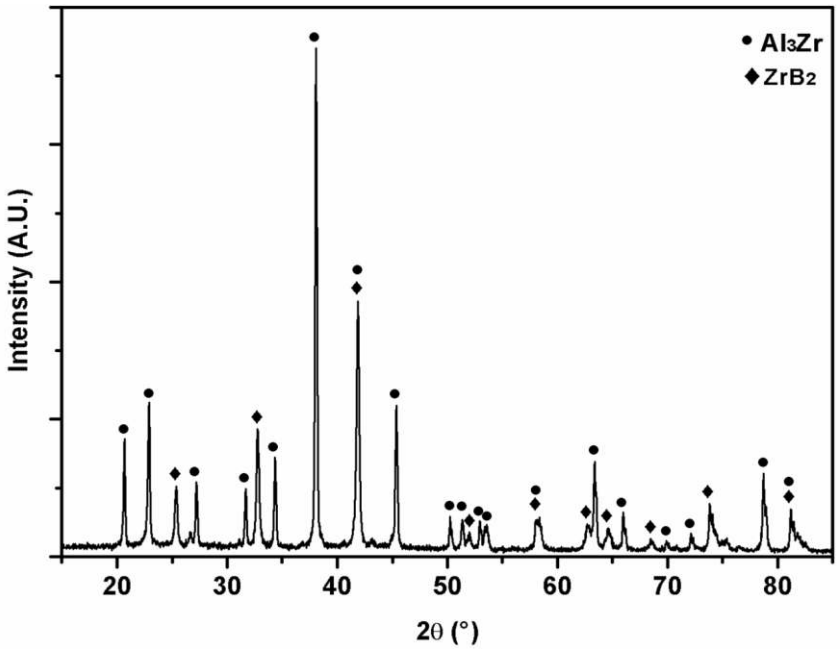

Figure 4.2 – XRD pattern of extracted particles from (ZrB_2+Al_3Zr)/Al-Mg composite [Gautam et al., 2016b].

4.4 Physical Properties

The values of density and porosity for all compositions have been evaluated and are listed in Table 4.6. The value of density increases with an increase in vol.% of ZrB_2 particles in the composites while porosity values are within a range of 5 to 6 vol.%.

Table 4.6 – The values of density and porosity in composites.

Composites	Density ($Kg/m^3 \times 10^3$)		Porosity (vol.%)
	Theoretical	Experimental	
C1	2.82	2.66	5.74
C2	2.86	2.71	5.11
C3	2.93	2.76	5.58
C4	2.99	2.81	6.09

4.5 Optical Microscopy

Figure 4.3 shows the optical micrographs of *insitu* composites. The micrograph of composite without ZrB_2 particles (C1) exhibits grains of matrix phase with uniformly distributed Al_3Zr particles in Fig. 4.3a. The micrographs of composites C2, C3 & C4 shown in Fig. 4.3b-d clearly indicate that the grain size of matrix phase refines with increasing amount of *insitu* formed ZrB_2 particles. Figure 4.4 shows the grain size distribution in different composites. The average grain size of Al-rich phase in C1 to C4 composites is 105.50, 71.42, 35 and 27.64 μm respectively. The refinement of grains may be due to restriction in the movement of solidification front due to the presence of ZrB_2 particles, and/or presence of ZrB_2 particles may also act as nucleation sites for matrix phase increasing the number of grains causing grain refinement. Dinaharan has also observed same phenomena for *insitu* formed ZrB_2 particles in AA6061 matrix composites [Dinaharan et al., 2011, Gautam and Mohan, 2015].

4.6 Electron Microscopy

Figure 4.5 shows the scanning electron micrographs of hybrid *insitu* composites with different vol.% of ZrB_2 particles. The micrograph in Fig. 4.5a of as cast composite

(without ZrB_2) consists of Al-rich matrix and Al_3Zr particles. Al_3Zr particles of polyhedron and rectangular shapes are uniformly distributed in the Al-rich matrix. Figure 4.5b-d shows the micrographs of composites reinforced with different vol.% of ZrB_2 particles. These micrographs clearly indicate the presence of larger size Al_3Zr particles along with clusters of ZrB_2 particles (much finer in size).

The number of clusters increase with increase in vol.% of ZrB_2 particles and this phenomenon also restricts the growth of Al_3Zr particles as evident from Fig. 4.5b-d. These clusters of particles become clearer at high magnification (Fig. 4.5e-f). Figure 4.6a-b shows the EDS analysis of cluster of ZrB_2 and Al_3Zr particle which further confirms the *insitu* formation of these particles. Figure 4.6c-d shows hexagonal and rectangular morphology of ZrB_2 particles. Tian et al. [2014] have also reported similar morphology of ZrB_2 particles reinforced in 2024 aluminium alloy. The different morphologies of ZrB_2 particles may be attributed to the fracture of columnar like particles formed in the melt during solidification [Tian et al., 2014].

Figure 4.7a-c shows the particle size histogram of Al_3Zr in Al_3Zr/Al-Mg composite, Al_3Zr in (Al_3Zr+ZrB_2)/Al-Mg composites and ZrB_2 in (Al_3Zr+ZrB_2)/Al-Mg composites. Al_3Zr particles in the Al_3Zr/Al-Mg composite are mostly within a size range of 6 to 29 μm as shown in Fig. 4.7a, whereas in (Al_3Zr+ZrB_2)/Al-Mg composites Al_3Zr particles are in the size range of 2.4 to 13.5 μm as shown in Fig. 4.7b. These figures clearly indicate a decrease in the size of Al_3Zr particles with incorporation of ZrB_2 particles. In Fig. 4.7c, most of the ZrB_2 particles are in a size range of 10-190 nm.

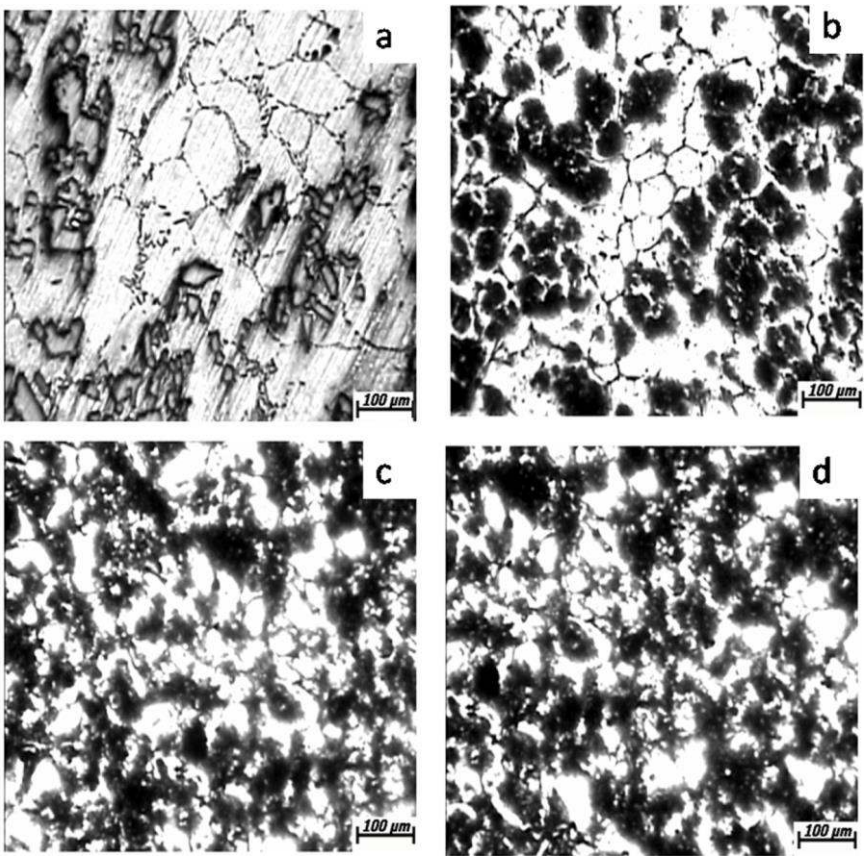

Figure 4.3 – Optical micrographs of (a) C1, (b) C2, (c) C3 and (d) C4 composites [Gautam and Mohan, 2015].

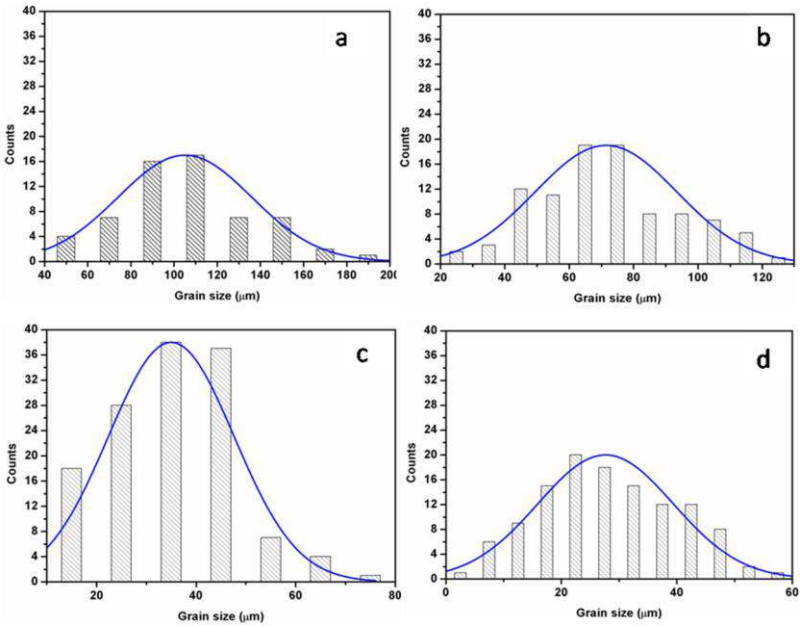

Figure 4.4 – Grain size distribution in (a) C1, (b) C2, (c) C3 and (d) C4 composites [Gautam and Mohan, 2015].

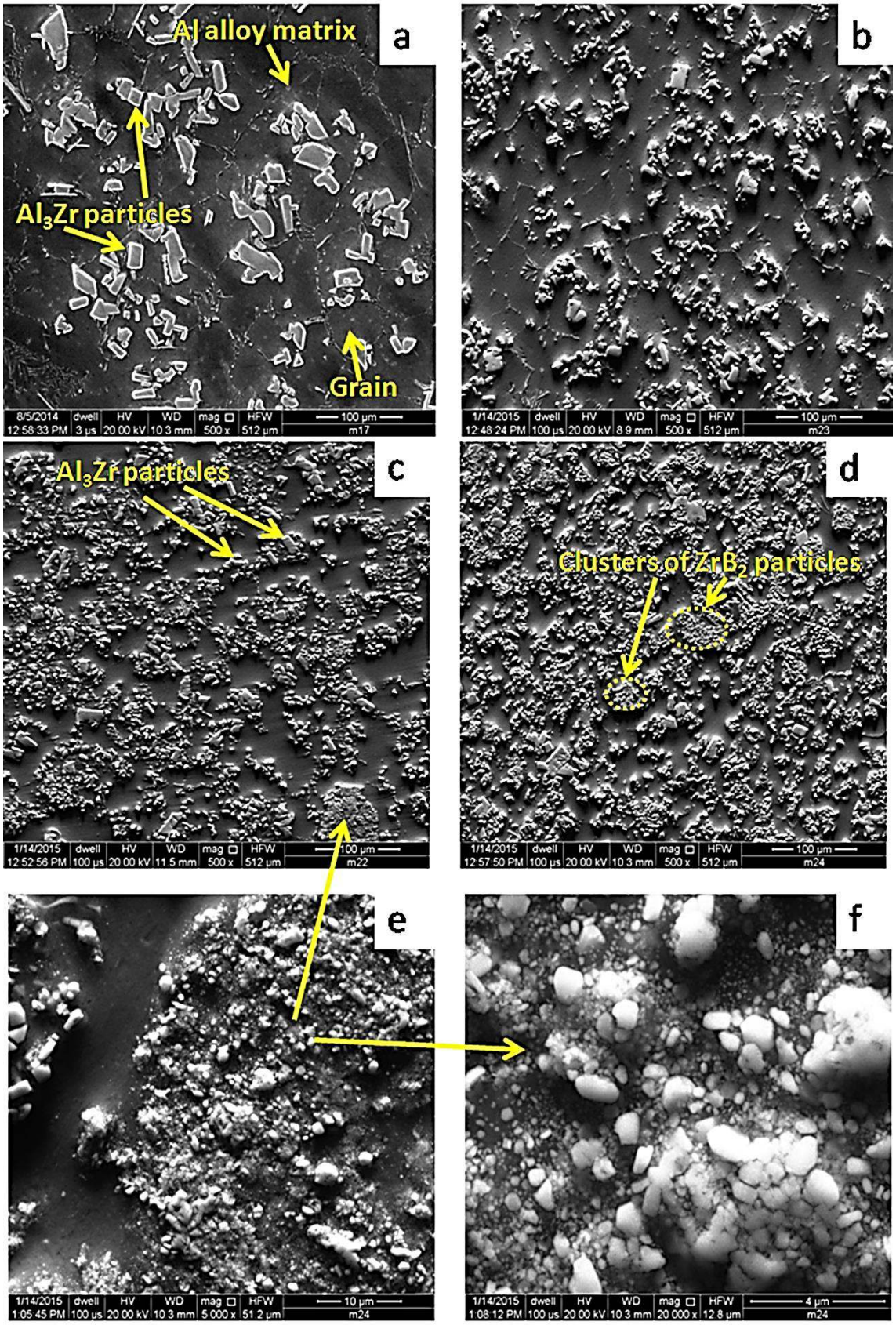

Figure 4.5 – Scanning electron micrographs of hybrid composites with different vol.% of ZrB_2 particles (a) C1, (b) C2, (c) C3, (d) C4, (e) & (f) clusters of ZrB_2 particles at higher magnification [Gautam and Mohan, 2015].

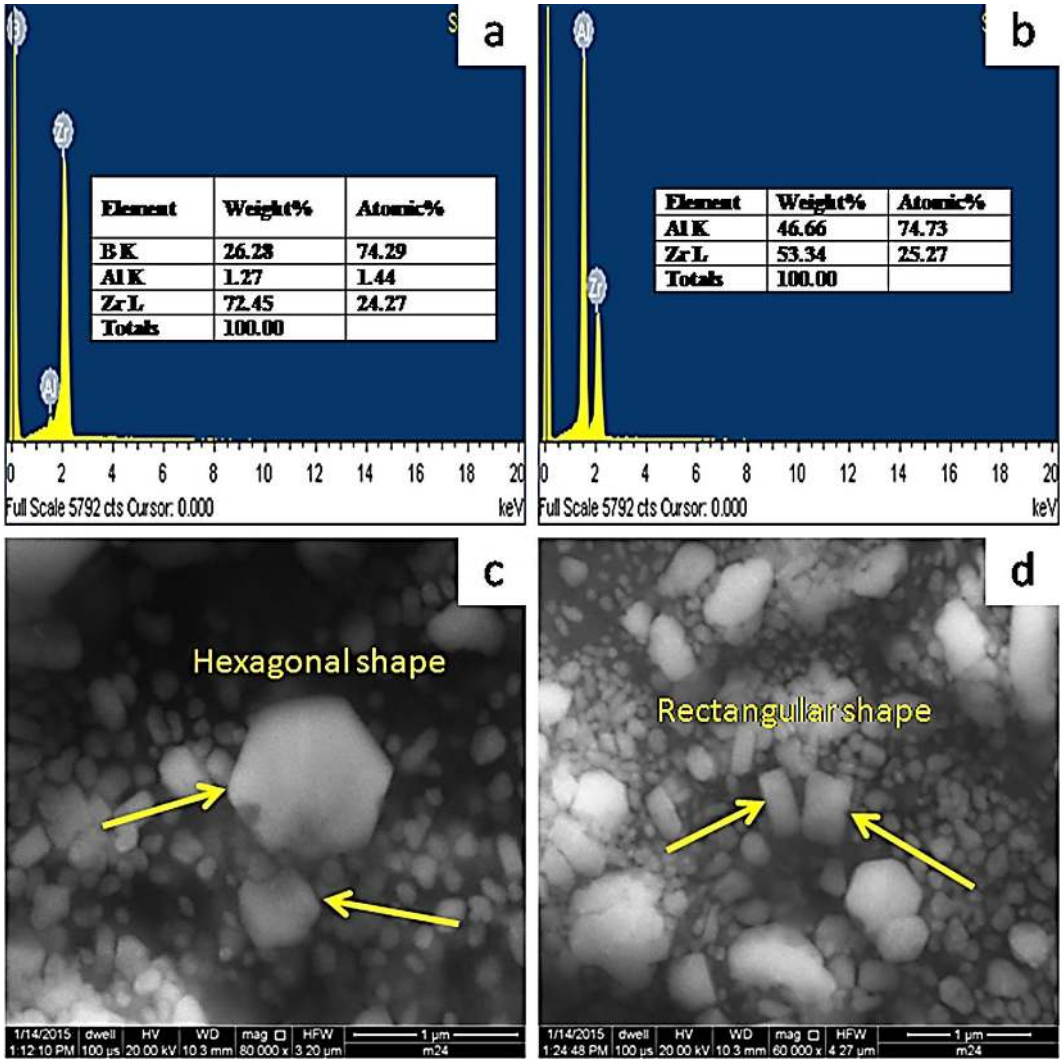

Figure 4.6 – (a) EDS pattern of cluster of ZrB_2 particles, (b) EDS pattern of Al_3Zr particle, (c) hexagonal ZrB_2 particles, and (d) rectangular ZrB_2 particles [Gautam and Mohan, 2015].

TEM micrographs in Fig. 4.8a-d show ZrB_2 morphology, dislocations near rectangular structure of ZrB_2 particle, diffraction pattern of ZrB_2 particles and matrix of the hybrid *insitu* composite respectively. The TEM micrograph in Fig. 4.8a confirms the hexagonal and rectangular morphology of ZrB_2 particles. The dislocations are not observed near the rectangular ZrB_2 particles (Fig. 4.8b) and interface is clear of any impurity in the form of oxides which is in agreement with Tian et al. [2014] work on ZrB_2 particle reinforced 2024Al matrix composites. The TEM diffraction pattern of ZrB_2 particle shown in Fig. 4.8c confirms that the crystal structure of ZrB_2 is hexagonal and space

group is P6/mmm, while Fig. 4.8d confirms the face centred cubic (fcc) structure of the matrix.

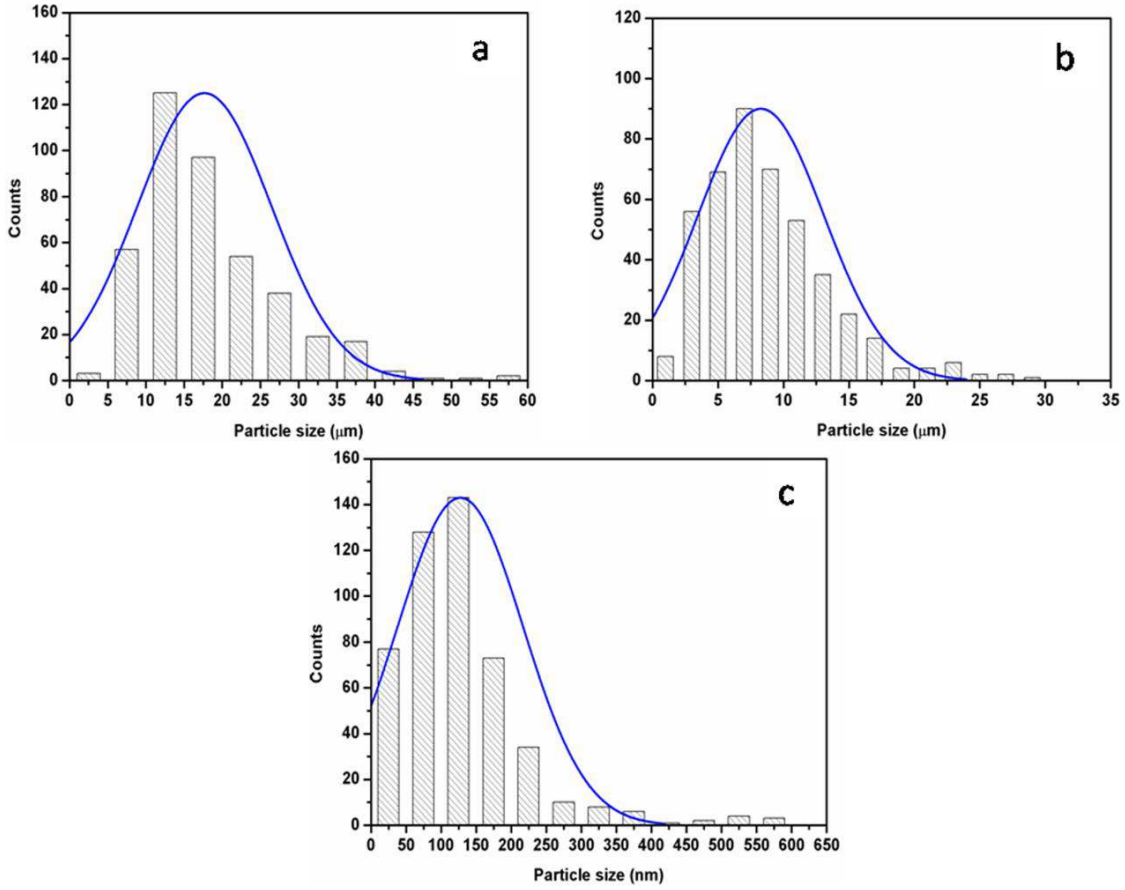

Figure 4.7 – Particle size histogram of (a) Al_3Zr in Al_3Zr/Al-Mg composite, (b) Al_3Zr in ((ZrB_2+Al_3Zr)/Al-Mg composites, and (c) ZrB_2 in ((ZrB_2+Al_3Zr)/Al-Mg composites [Gautam and Mohan, 2015].

Figure 4.9a-b shows the TEM micrograph of Al_3Zr particle and its electron diffraction pattern. The Fig. 4.9a shows that Al_3Zr particles are present in the form of facets whereas diffraction pattern in Fig. 4.9b confirms that the crystal structure of Al_3Zr is body centred tetragonal structure (BCT) and space group is I4/mmm. TEM micrograph in Fig. 4.10 clearly exhibits the presence of dislocations in the matrix of the hybrid (Al_3Zr+ZrB_2)/Al-Mg composite. These dislocations are generated due to the mismatch in coefficient thermal expansion between the reinforcement particles and the matrix

alloy while fabricating composites. This phenomenon has been observed by other workers also in different system such as fabrication of Al nano-composites reinforced with Al_2O_3 and Al_3Zr particles via magneto-chemical melt reaction technique [Zhao et al., 2008, Gautam and Mohan, 2015].

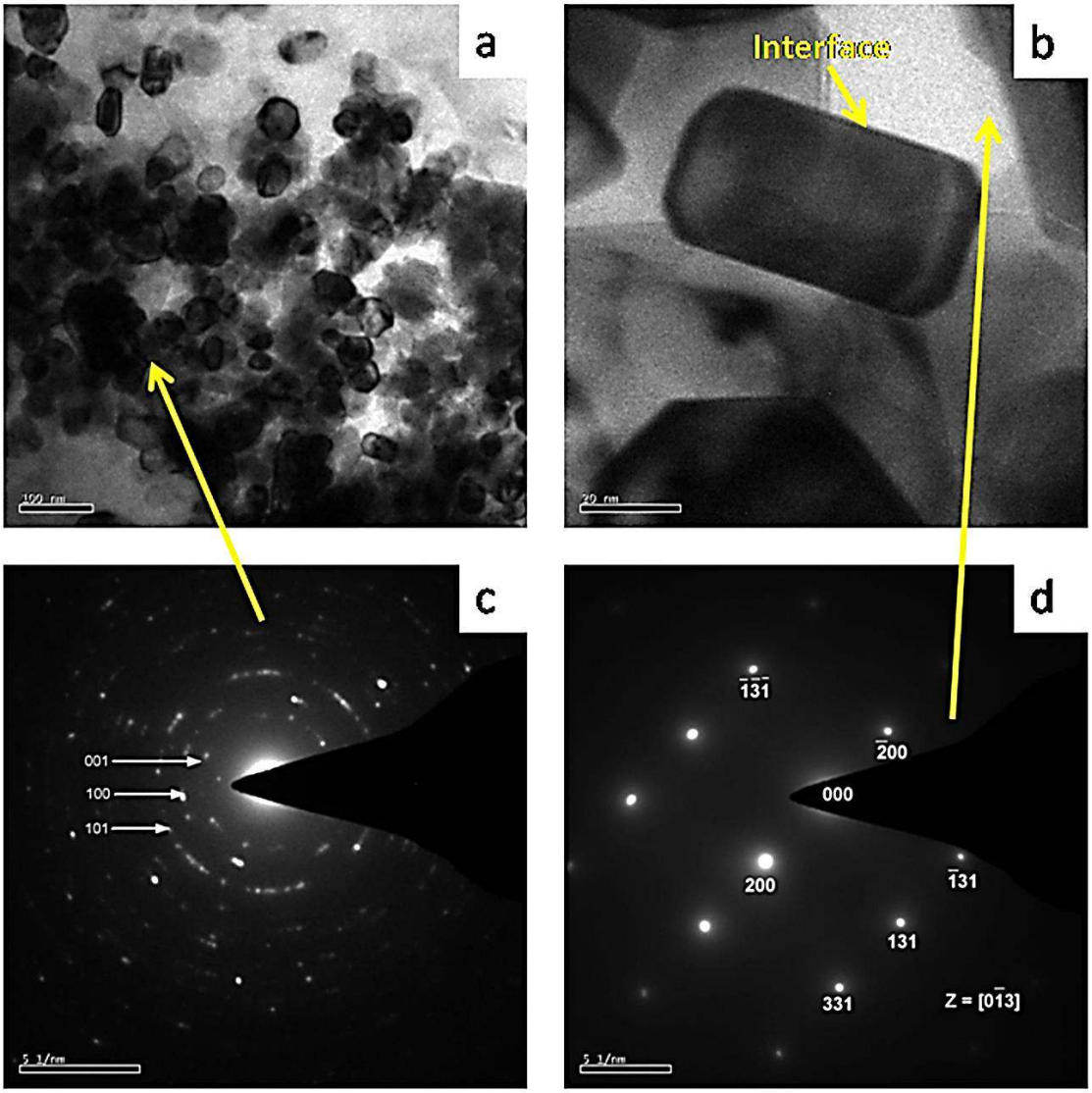

Figure 4.8 – TEM Micrographs of hybrid composite: (a) rectangular and hexagonal ZrB_2 particles, (b) dislocation free region near ZrB_2 particle, (c), diffraction patterns of ZrB_2 particles and (d) diffraction pattern of matrix [Gautam and Mohan, 2015].

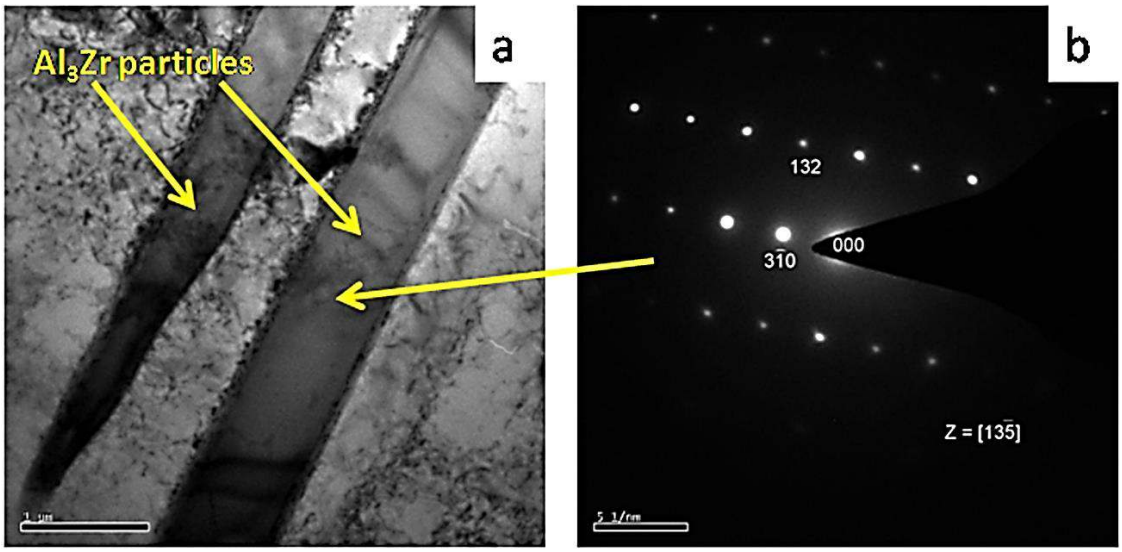

Figure 4.9 – TEM Micrographs of hybrid *insitu* composite (a) rectangular Al_3Zr particle and (b) diffraction pattern of Al_3Zr particle [Gautam and Mohan, 2015].

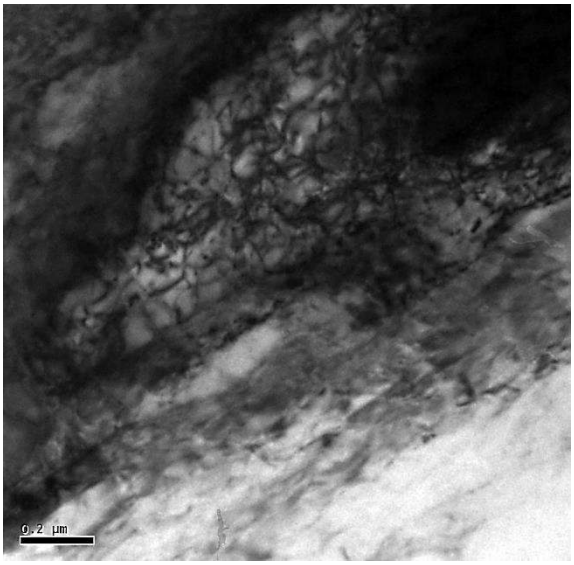

Figure 4.10 – TEM Micrographs showing the dislocation in the matrix of hybrid composite [Gautam et al., 2016b].

4.7 Mechanical Properties and Fractography

Figure 4.11 shows the engineering stress-strain curves of as cast (Al_3Zr+ZrB_2)/Al-Mg composites reinforced with different vol.% of ZrB_2 particles tested at room temperature. The values of ultimate tensile strength (UTS), yield strength (YS) and percentage

elongation have been evaluated and plotted in Fig. 4.12. The strength parameters i.e ultimate tensile strength and yield strength improve with increase in the vol.% of ZrB_2 particles up to 3 vol.% but beyond this percentage of ZrB_2 particles UTS and YS observe a decreasing trend. However, it is interesting to note that unlike many *exsitu* composites, in the present study percentage elongation improves with *insitu* formation of 1 vol.% ZrB_2 particles in the composite (C2) as compared to 10 vol.% Al_3Zr/Al-Mg composite (C1). But further addition of ZrB_2 particles leads to decrease in % elongation (C3, C4 in Fig. 4.12). The improvement in the percentage elongation in C2 as compared to C1 may be due to the grain refining effect, as also reported by other workers [Ramesh et al., 2010; Tian et al., 2014]. They observed the same behavior in 6063Al and 2024Al alloys reinforced with TiB_2 and ZrB_2 respectively.

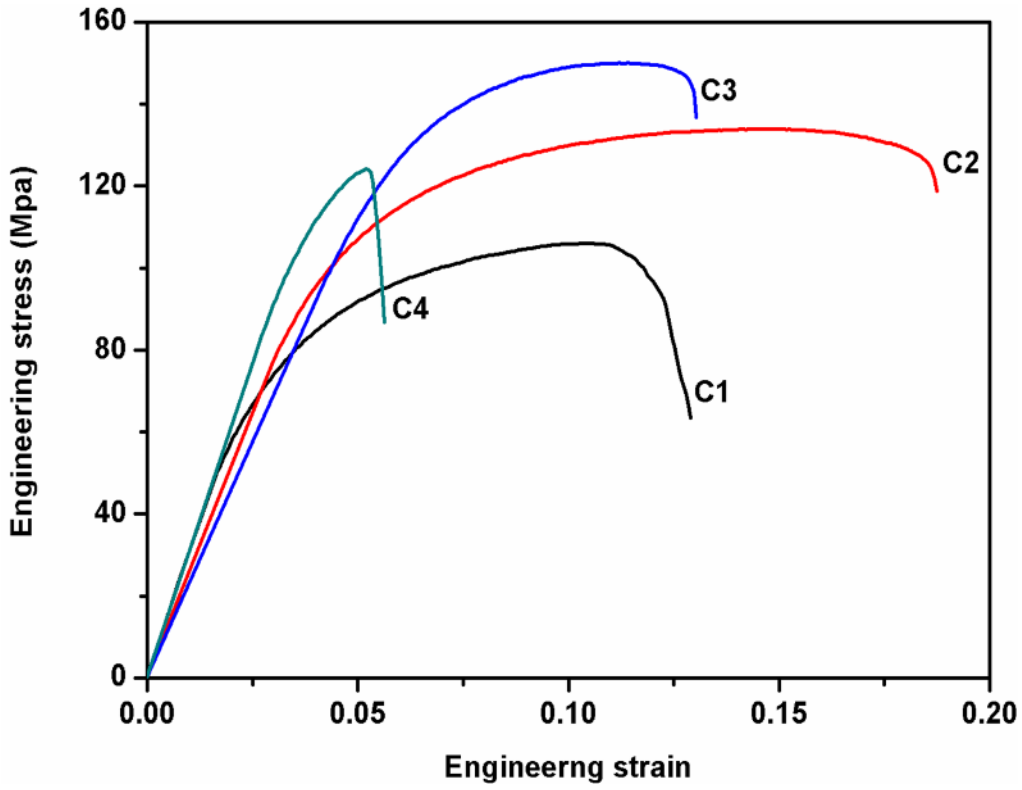

Figure 4.11 – Engineering stress-strain curves of the composites [Gautam and Mohan, 2015].

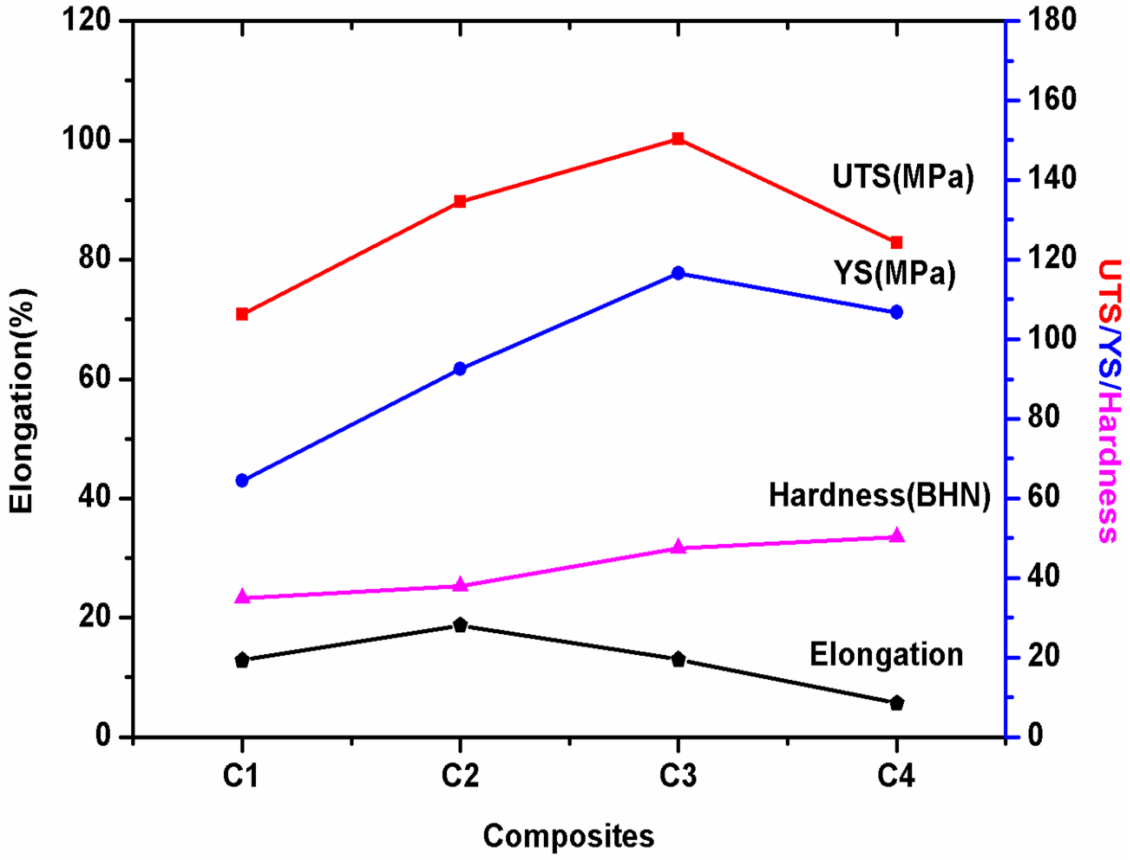

Figure 4.12 – Variation of mechanical properties in composites [Gautam and Mohan, 2015].

In such composites two phenomena work simultaneously i.e. strengthening due to grain refinement (Fig. 4.3a-d) and Orowan strengthening due to the interaction of dislocations with the dispersed hard particles. When the composite material is under plastic deformation, hard ZrB_2 particles act as a barrier to hinder the motion of dislocations. This strengthening effect of particles in the alloy matrix increases with increase in the vol.% of particles. The strength parameters are adversely affected beyond a certain vol.% of particles. In the present case this limiting vol.% of ZrB_2 particles is 3. It may be due to the generation of greater number of crack nucleation sites due to debonding of

ZrB_2 clusters causing early failure as also observed by Mandal et al. [2008] in case of steel fiber reinforced Al-2Mg alloys.

Further, to understand flow curve properties true stress vs. true plastic strain has been plotted on log–log scale in Fig. 4.13 and strain hardening exponent & strength coefficient of as cast composites have been plotted in Fig. 4.14. The strain hardening exponent is calculated from the slopes of the plots and the strength coefficient is calculated from the intercept on y axis at $\varepsilon_p = 1$. It is seen that strength coefficient increases with increase in ZrB_2 particles in the composites, while the strain hardening decreases. This phenomenon is observed up to 3 vol.% ZrB_2 in the hybrid composite, and beyond that strength coefficient decreases and strain hardening increases which could be due to the presence of ZrB_2 particles clusters in the composite.

Percentage elongation in the present investigation improves by about 50% with a meager amount of 1 vol. % ZrB_2 (Fig. 4.12; C2 composite) which may be due to the grain refinement (Fig. 4.3). Fine grains may retard the propagation and growth of crack. Further, fracture of C1 in Fig. 4.15a shows facets of Al_3Zr particles and dimples of matrix, but in C2 (Fig. 4.15b) large number of smaller dimples due to refining of grains are seen which is in agreement with tensile results. Ramesh et al. [2010] and Tian et al. [2014] also observed same behavior in different composites. However, with increase in ZrB_2 particles for C3 and C4, percentage elongation decreases which could be due to the debonding of clusters of ZrB_2 particles causing voids in the ductile matrix, hence, crack propagates easily leading to early failure. Corresponding fractographs in Fig. 4.15c-e confirm the results showing quasi cleavage fracture and debonding of ZrB_2 clusters.

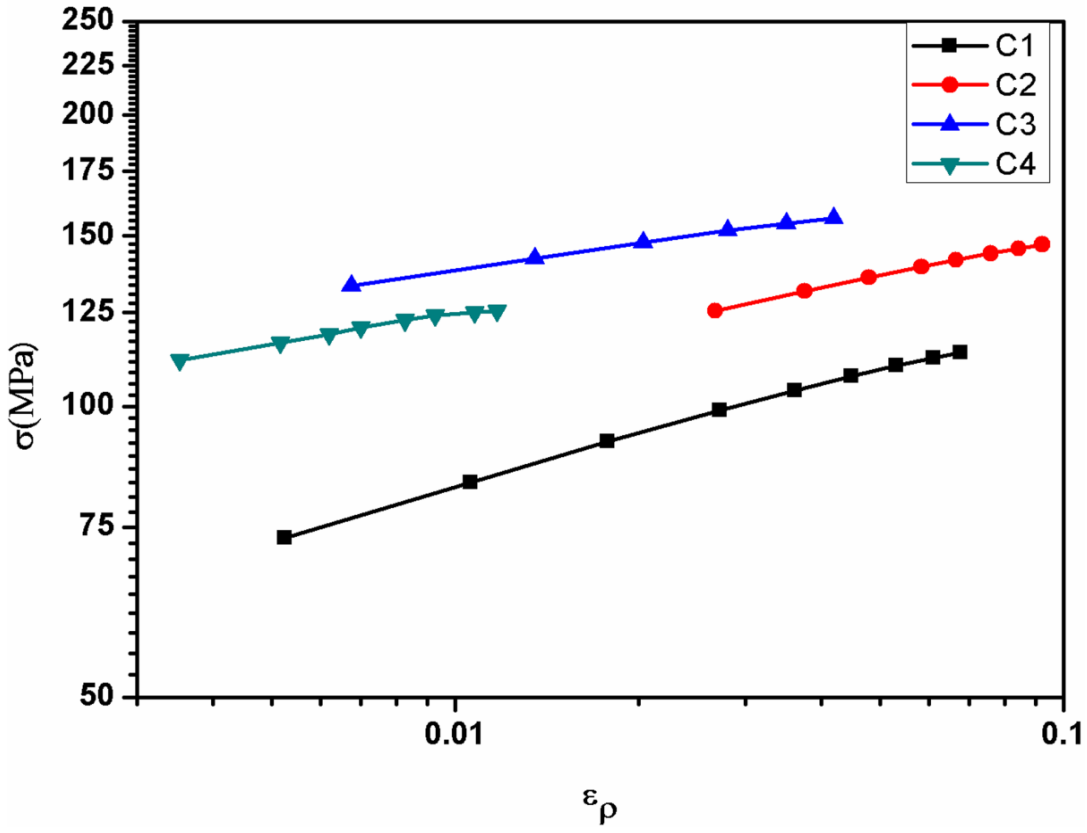

Figure 4.13 – σ vs. ε_ρ plots on log scale of composites [Gautam and Mohan, 2015].

The variation in bulk hardness (BHN) with vol.% of ZrB_2 particles in as cast (Al_3Zr+ZrB_2)/Al-Mg composites is shown in Fig. 4.12. The improvement in hardness with increase in vol.% of ZrB_2 particles may be attributed to the generation of dislocations during solidification which increase with increase in the amount of hard ZrB_2 particles. These dislocations act as a barrier to plastic deformation, therefore, hardness increases. Maximum hardness has been observed for C4 composite with 5 vol.% of ZrB_2 particles which is almost 1.5 times of the hardness of C1 (which doesn't have ZrB_2 at all). The summarized data of mechanical properties of composites is given in Table 4.7 [Gautam and Mohan, 2015].

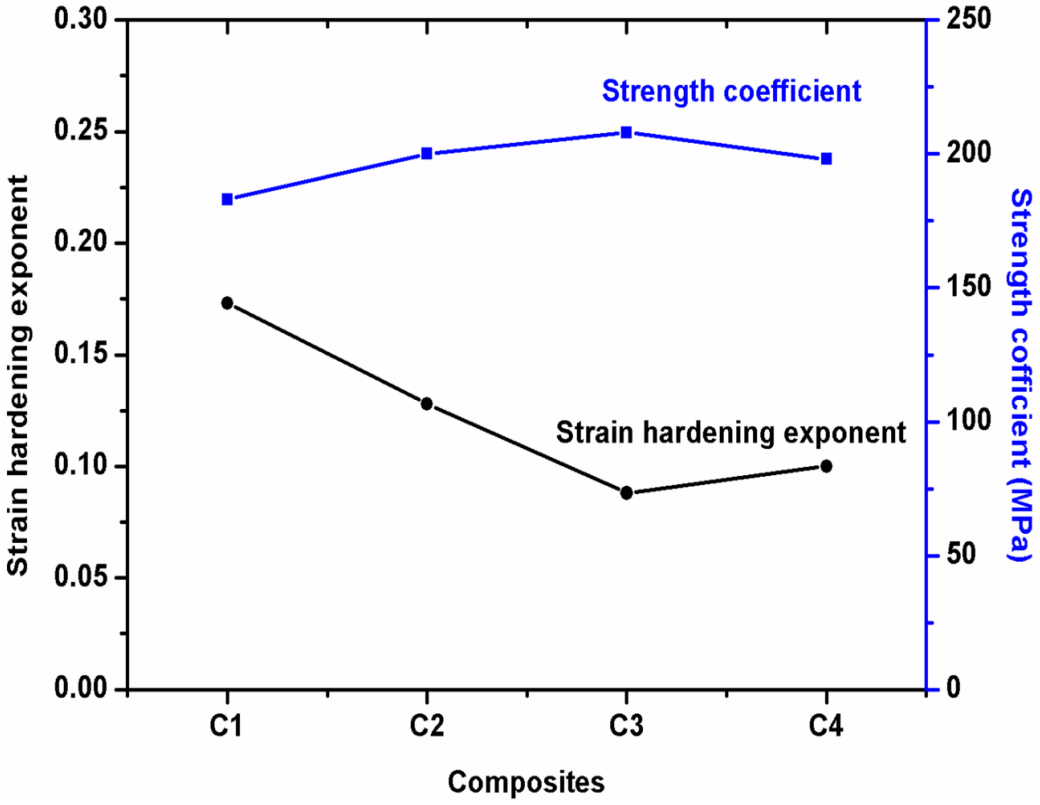

Figure 4.14 – Variation of flow curve properties of composites.

To find out the contribution of different strengthening mechanisms (i.e. dislocation, solid-solution, grain refinement and Orowan strengthening) in hybrid composites, a detailed study has been conducted and discussed in subsequent sections.

4.8 Strengthening Mechanism

The strengthening in hybrid (ZrB_2+Al_3Zr)/Al-Mg composites is likely to take place due to the different mechanisms such as dislocation, Orowan, grain refinement, and solid solution. Therefore, the contribution of each strengthening mechanism gives the overall strength of composites,

$$\sigma_{composite} = \Delta\sigma_{dislocation} + \Delta\sigma_{Orowan} + \Delta\sigma_{grain-refinement} + \Delta\sigma_{solid-solution} \quad (4.3)$$

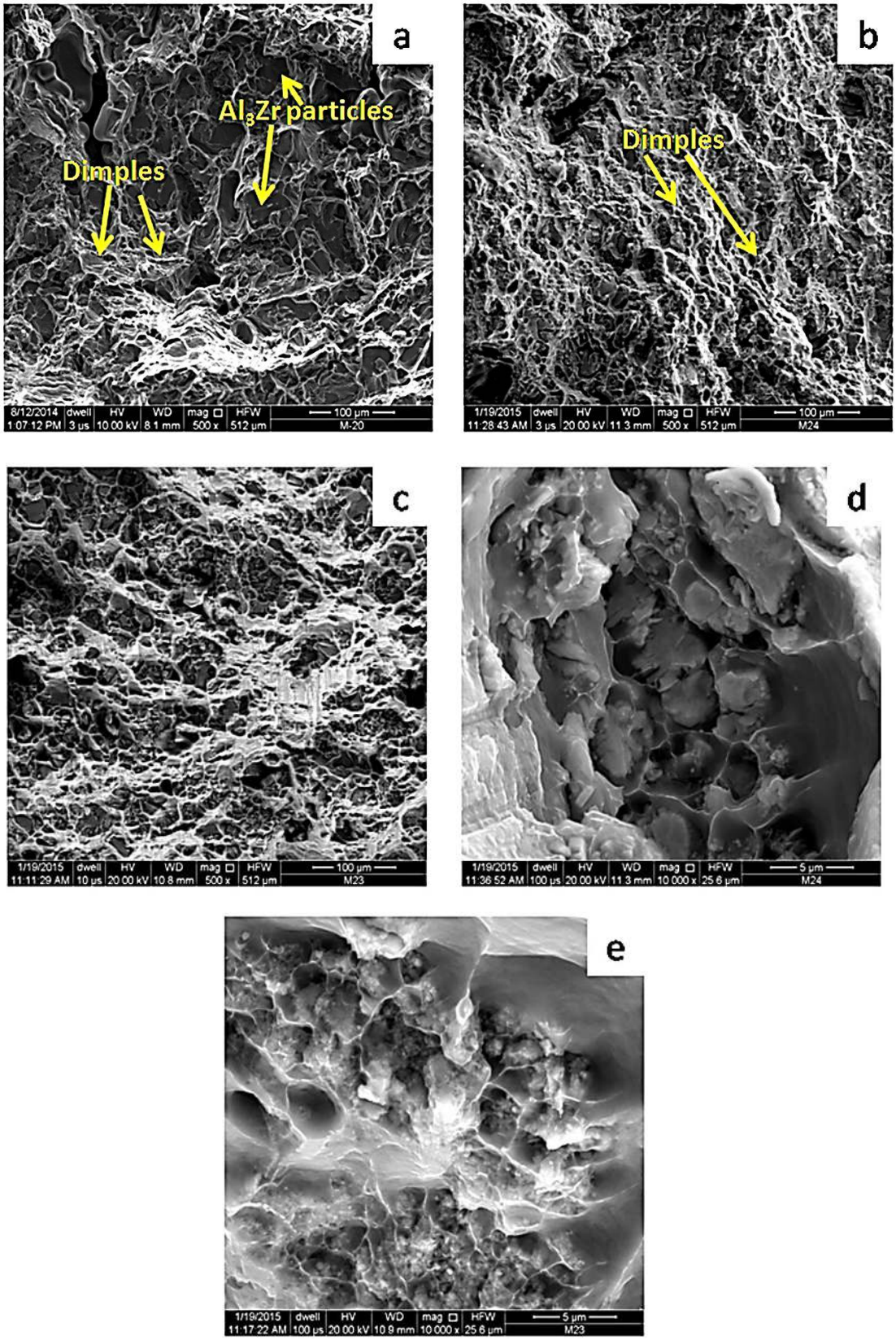

Figure 4.15 – Fractographs of (a) C1, (b) C2, (c) C4, (d) and (e) show the debonding of ZrB_2 clusters in C4 composite [Gautam and Mohan, 2015].

Table 4.7 – Summarized data of mechanical properties of composites.

Composites	Strength parameters (MPa)		Elongation (%)	Hardness (BHN)	Flow curve parameters	
	UTS	YS			Strain hardening exponent, n	Strength coefficient, K(MPa)
C1	106.2	64.4	12.88	35.00	0.173	183
C2	134.5	92.5	18.74	38.00	0.128	200
C3	150.3	116.5	13.01	47.47	0.088	208
C4	124.2	106.7	5.62	50.32	0.100	198

The physical meaning of different terms used and their values used to calculate the contribution of different strengthening mechanisms are tabulated in Table 4.8. The contribution of each strengthening mechanism is discussed in subsequent sections.

Table 4.8 – The different terms and their meaning used in the evaluation of different strengthening mechanisms [Gautam et al., 2016b].

Terms	Meaning	Values
G	Shear modulus of Al-Mg alloy	25.9 GPa [Handbook ASMVol. 2, 1990]
b	Magnitude of Burger's vector	$\sqrt{2}/_{2a}$= 0.286 nm, where, a (lattice constant) = 0.405 nm for fcc Al [Ma et al., 2014]
v	Poisson ratio of Al-Mg alloy	0.33 [Handbook ASMVol. 2, 1990]
K_H	Hall-Petch coefficient	0.06 $MPam^{1/2}$ [Thangaraju et al., 2012]

4.8.1 Dislocation Strengthening

In this subsection the contribution of dislocations to yield strength has been calculated. The dislocations in the cast composites are generated during solidification of

composites due to the difference in coefficient of thermal expansion (CTE) of matrix and reinforced Al_3Zr and ZrB_2 particles. Figure 4.10 shows the presence of dislocations in the Al-rich matrix of a hybrid (Al_3Zr+ZrB_2)/Al-Mg composite. The generation of dislocation is also reported by Zhao and Sun [2001] in the hybrid Al matrix composites reinforced with Al_2O_3 and Al_3Zr particles synthesized by magneto-chemical melt reaction technique. They further reported that the dislocation generation is also affected by the reinforcement particle size and their volume fraction, matrix strength, and CTE. Thus, increase in the dislocation density in composites increases their yield strength. The contribution of dislocations to yield strength [Clyne and Withers, 1991] in hybrid C2 and C3 composites has been calculated by following equation –

$$\Delta\sigma_{dislocation} = AGb\sqrt{\rho} \tag{4.4}$$

Where, A is the fractional surface area of reinforced particles in the composites, G is the shear modulus of Al-Mg matrix alloy, b is the magnitude of Burger's vector and ρ is the dislocation density of the hybrid composites.

The crystallite size (d) and lattice strain (ε) of the hybrid composite samples are required to calculate the dislocation density. These parameters have been evaluated by Williamson-Hall method [Williamson and Hall, 1953] as given in following equation –

$$B\cos\theta_B = \frac{K_c\lambda}{d} + \varepsilon\sin\theta_B \tag{4.5}$$

Where, B is the true peak broadening, λ is the wave length of CuKα incident radiation (λ = 1.5405 Å), K_c is about 0.9 and θ_B is the Bragg angle. The true peak broadening B is defined as –

$$B = \sqrt{B^2_{observed} - B^2_{instrument}} \quad (4.6)$$

Where, $B_{observed}$ is the observed peak broadening in hybrid composites and $B_{instrument}$ is the broadening due to the instrument. The value of $B_{observed}$ has been calculated by the XRD pattern of hybrid composites shown in Fig. 4.1 and has been used in the eqn. (4.6). After calculating the value of true peak broadening B, liner fitted curve between B $\cos\theta_B$ vs. $\sin\theta_B$ was drawn and values of slope and intercept were obtained to give crystallite size and lattice strain in the hybrid composites. The dislocation density [Zhao et al., 2004] in hybrid composites is defined in terms of d and ε as,

$$\rho = \frac{2\sqrt{2\varepsilon}}{db} \quad (4.7)$$

Where, b is the Bergers vector which is defined as $\sqrt{2}/2a$ in terms of lattice constant for fcc crystal structure. The calculated value of Burger vector is 0.405 nm for fcc aluminium. With the help of crystallite size and lattice strain, the dislocation density has been calculated from eqn. (4.7), and the values for C2 and C3 composites are 1.93×10^{14} and 2.63×10^{14} respectively which are further used to calculate the contribution of dislocation strengthening in the yield strength of different composites.

Fractional surface areas calculated for composite C2 and C3 are 0.169 and 0.173 respectively. The values of G and b are taken from Table 4.8 and the dislocation density has been found out from XRD analysis. The calculated values for yield strength are 17 and 21 MPa for C2 and C3 composites respectively [Gautam et al., 2016b].

4.8.2 Orowan Strengthening

Contribution of Orowan strengthening to yield strength of hybrid composites has been quantified in this subsection. Orowan strengthening occurs from the interaction of

distributed hard reinforcement particles and dislocations. The *insitu* formed ZrB_2 and Al_3Zr particles act as barrier in the movement of dislocations. The resistance to propagation of dislocation under plastic deformation during tensile loading leads to increase in the strength of composites. This resistance increases with increasing vol.% of reinforced particles and results in further increase in the strength of composites.

The contribution of Orowan strengthening to yield strength [Tong and Ghosh, 2001] in hybrid C2 and C3 composites is calculated by the following equation,

$$\Delta\sigma_{orowan} = \frac{2Gb}{2\pi\sqrt{(1-\upsilon)}}\frac{1}{\lambda_e}\ln(D/b) \quad (4.8)$$

Where, G is the shear modulus of Al-Mg matrix alloy, b is the magnitude of Burgers vector, υ is the Poisson ratio of the matrix, D is the average diameter of reinforcement particles, and λ_e is the edge to edge particle spacing in the composites. The edge to edge particle spacing (λ_e) in the composites [Tong and Ghosh, 2001] is described as-

$$\lambda_e = D\sqrt{\left(\frac{\pi}{6V_f} - \frac{2}{3}\right)} \quad (4.9)$$

Where, D is the average particle diameter, and V_f is the volume fraction of reinforced particles in the composites.

The values of G, b and υ have been taken from Table 4.8. The particle size distribution of Al_3Zr and ZrB_2 in the composites as shown in Fig. 4.7b-c give an average value of 11.31 μm for Al_3Zr and 95.13 nm for ZrB_2. The volume fractions of ZrB_2 and Al_3Zr particles in both C2 and C3 composites are given in Table 4.5. After calculating λ_e values for both the composites using eqn. (4.9), and the Orowan strengthening contribution from eqn. (4.8), the YS values are obtained as 25 and 43 MPa for C2 and C3 hybrid composite respectively [Gautam et al., 2016b].

4.8.3 Grain-refinement Strengthening

The contribution of grain refinement to yield strength of hybrid composites has been presented here. The grain-refinement strengthening occurs due to the interaction of dislocations with grain boundaries. The second phase reinforcement particles in the composites act as nucleation sites for matrix phase and restrict the solidification process, causing the grain refinement. The refinement of Al-rich grains increases the density of grain boundaries and the resistance to motion of dislocations, thereby contributing to strength. The grain-refining strengthening is improved with increasing volume fraction of reinforcement particles. Figure 4.3b-c clearly indicates that the reinforcement particles refine the matrix grains and magnitude of refinement increases with increasing vol.% of reinforcement particles in the hybrid composites. The contribution of grain-refinement strengthening to yield strength [Zhao et al., 2008] in hybrid C2 and C3 composite has been calculated by the following equation –

$$\Delta\sigma_{grain-refinement} = K_H {d_g}^{-1/2} \quad (4.10)$$

Where, K_H is the Hall-Petch coefficient of the Al-Mg base alloy, and d_g is the average grain size of the matrix in the hybrid composites.

The value of K_H has been taken from Table 4.8. The grain size distribution in the composites is shown in Fig. 4.4b-c with an average value of 71.42 and 35 μm for C2 and C3 hybrid composites respectively. From eqn. (4.10) the contribution of grain-refining strengthening comes out to be 7 and 10 MPa for C2 and C3 hybrid composites respectively [Gautam et al., 2016b].

4.8.4 Solid-solution Strengthening

The contribution of solid-solution strengthening to yield strength of hybrid composites has been presented in this sub-section. The solid-solution strengthening occurs as a result of interaction between local strain field and dislocations. The local strain field is developed when other elements are alloyed with a metal matrix as solute atoms with difference in atomic size and shear modulus from matrix. This strain field interacts with dislocations and resists their motion, therefore, the yield strength of composites increases. The contribution of solid-solution strengthening to yield strength [Zhao et al., 2008] in hybrid C2 and C3 composites is calculated as –

$$\Delta\sigma_{solid-solution} = G\varepsilon_d\sqrt{x_f/4} \quad (4.11)$$

Where, G is the shear modulus of matrix and ε_d is the fractional difference in zirconium and aluminium atom diameters, and x_f is the fractional concentration of foreign atoms.

The value of G has been taken from Table 4.8 and ε_d has been calculated as 0.119. The calculated values of x_f are 0.0991 and 0.1158% for C2 and C3 hybrid composites respectively. On substituting these values of G, ε_d and x_f in eqn. (4.11), the contribution of solid-solution strengthening is found to be 49 and 52 MPa for C2 and C3 composites respectively [Gautam et al., 2016b].

4.8.5 Summary of Strengthening Mechanism

The contribution of each strengthening mechanism is summarized in Table 4.9. It is observed that the predicted yield strength of hybrid composites is nearly 5 to 8% higher than the experimental ones, which could be due to the clustering of ZrB_2 particles in the composites. The inter-particle bonds in clusters are weaker as compared to those between ceramic and matrix, therefore, the intrinsic strength of the indivisible particles

is higher. Hence, the clustering constitutes the defects that can initiate early failure. Among all mechanisms solid-solution and Orowan are the predominant strengthening mechanisms as it is obvious from Fig. 4.16 [Gautam et al., 2016b].

Table 4.9 – Contribution of different strengthening mechanisms to predicted yield strength in hybrid composites and experimental yield strength [Gautam et al., 2016b].

Composites	Yield strength (MPa)					
	Experimental	Predicted contribution				
		Dislocation	Orowan	Grain-refining	Solid-solution	Total
C2	93	17	25	7	49	98
C3	117	21	43	10	52	126

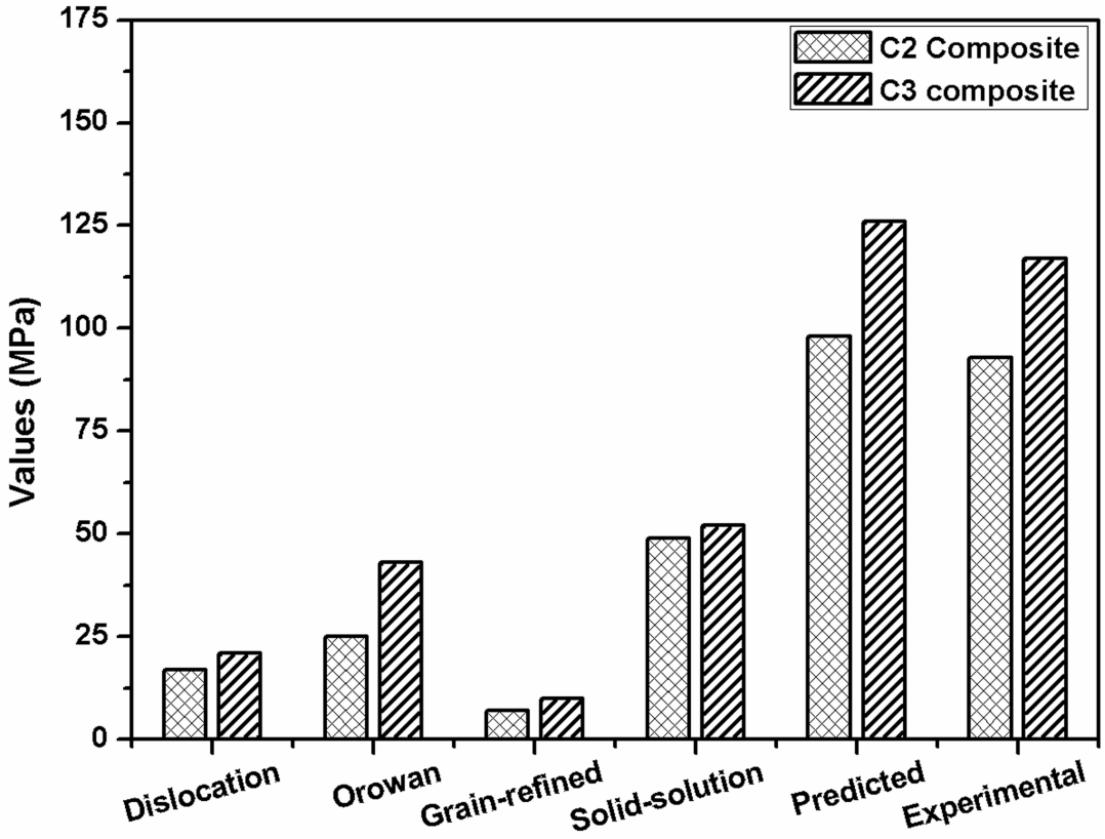

Figure 4.16 – Contribution of different strengthening mechanisms in hybrid composites and comparison of predicted yield strength with experimental yield strength.

4.9 Tribological Properties

To see the effect of vol.% of ZrB_2 particles on the dry sliding wear and friction behaviour of Al_3Zr/Al-Mg composite, the dry sliding wear test is carried out at different combinations of operating parameters, such as sliding distance, normal load and sliding velocity for all composites. Worn surfaces have been studied under SEM with EDS and profilometer. The wear and friction results have been correlated with the worn surface analysis.

4.9.1 Effect of Sliding Distance

Effect of sliding distance on cumulative mass loss and coefficient of friction (COF) for C1 to C4 composites at 20 N normal load and 1 m/s sliding velocity is shown in Fig. 4.17. It is observed that the cumulative mass loss increases linearly with sliding distance for all the composites. Almost a linear relationship between cumulative mass loss with sliding distance indicates a steady state wear (Fig. 4.17a), while COF shows a fluctuating tendency with sliding distance (Fig. 4.17b) for all composites.

4.9.2 Effect of Load

The variation of wear rate, wear rate per unit vol.% of reinforcement and coefficient of friction (COF) with normal load for all composites at 1 m/s sliding velocity is shown in Fig. 4.18. Wear rate per unit vol.% of reinforcement gives a measure of load bearing capacity with increasing hard particles. It is observed that wear rate and wear rate per unit vol.% of reinforcement continuously increases with increase in normal load for all composites, while COF shows a decreasing trend with increasing normal load for all composites.

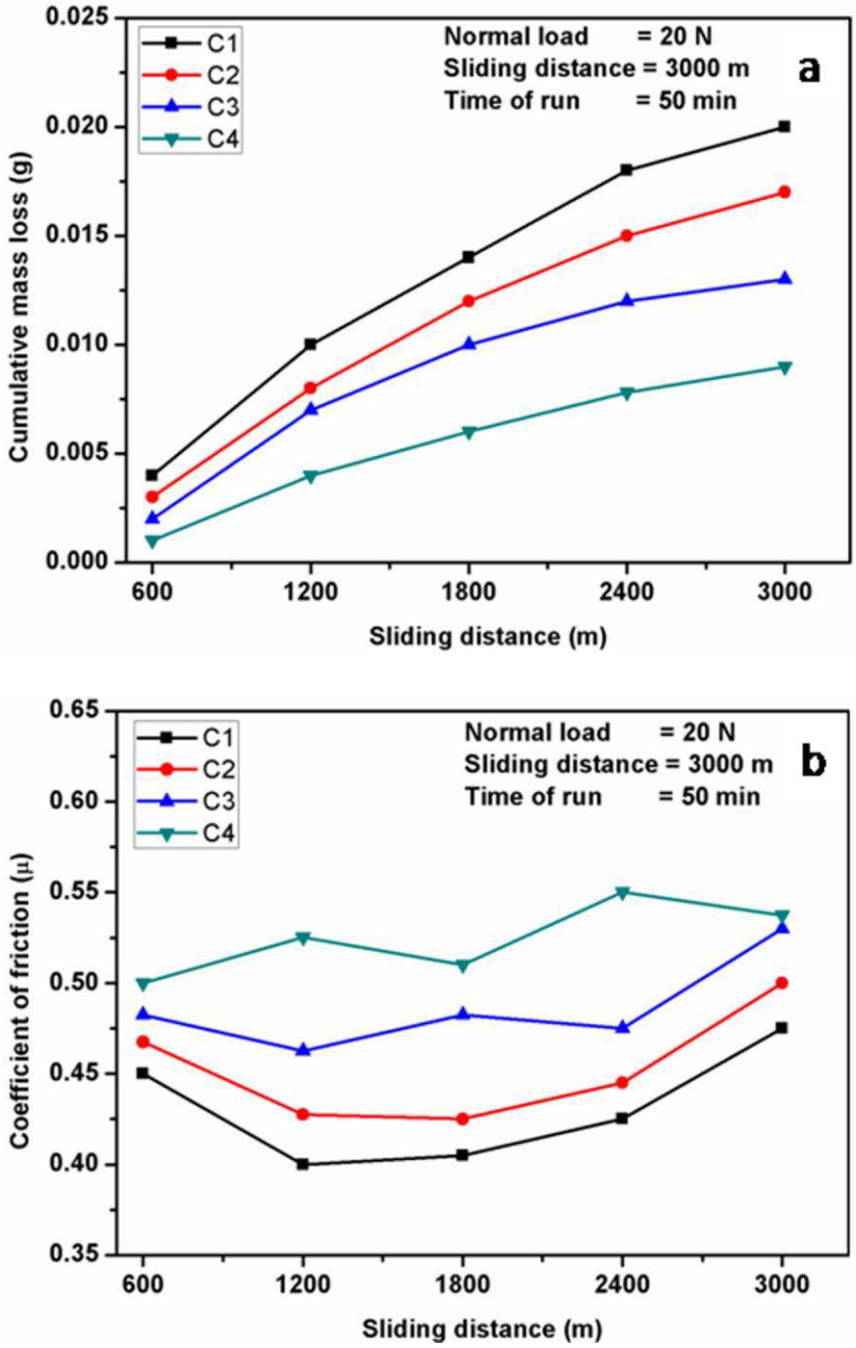

Figure 4.17 – Variation of (a) cumulative mass loss and (b) coefficient of friction with sliding distance.

4.9.3 Effect of Sliding Velocity

The variation of wear rate, wear coefficient and coefficient of friction (COF) with sliding velocity for all composites at 20 N normal load is shown in Fig. 4.19.

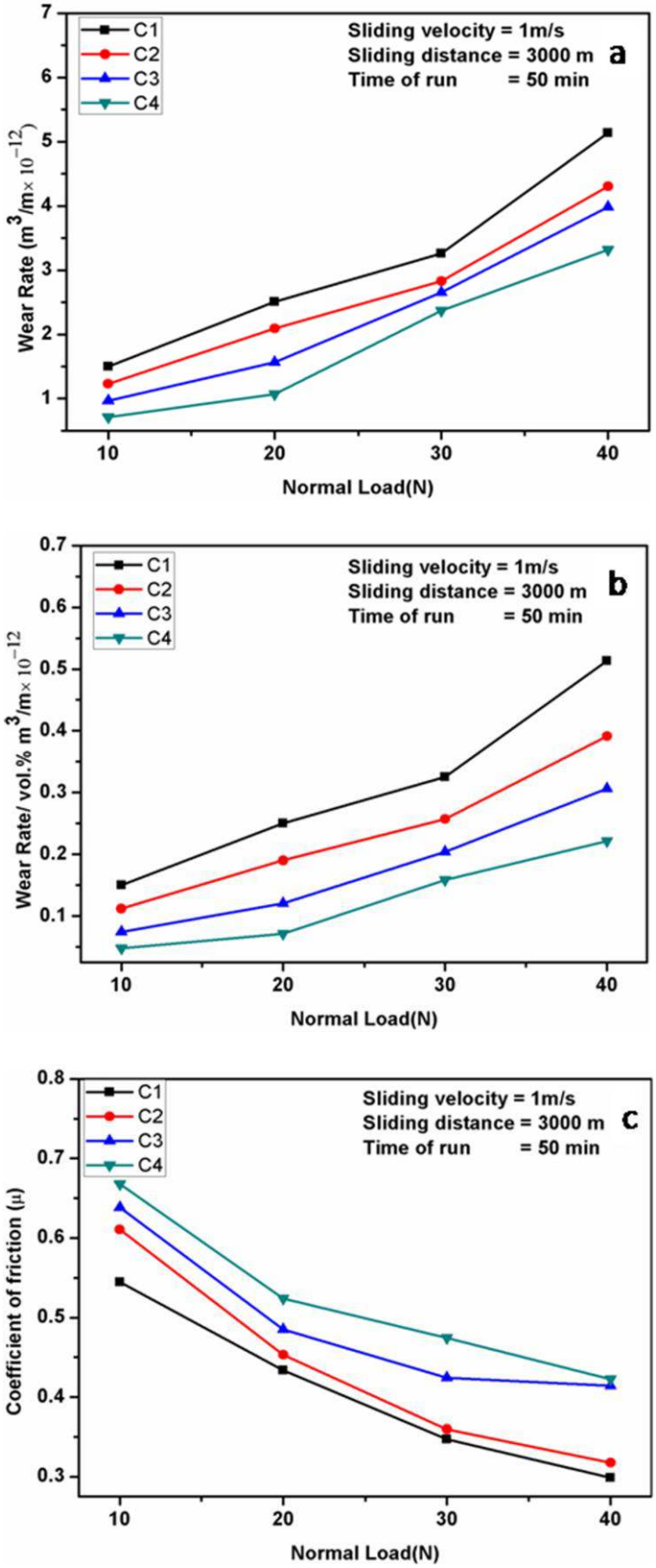

Figure 4.18 – Variation of (a) Wear rate, (b) wear per unit vol.% reinforcement, and (c) coefficient of friction with different normal load.

Wear coefficient indicates the load bearing capacity. It is observed that wear rate of C2, C3 and C4 composites shows entirely different behavior from the composite without ZrB_2 (C1). For C1, wear rate initially decreases but beyond 2.5 m/s sliding velocity it increases sharply, while for C2, C3 and C4 wear rate initially increases slightly which is followed by a marginal decrease after 2 m/s sliding velocity (Fig. 4.19a). It is interesting to report that at high sliding velocity; wear rate of hybrid composites is much lower than C1. Wear coefficient also shows the same trend (Fig. 4.19b). These figures indicate that hybrid composites can be successfully used even at higher velocities. It is also observed that coefficient of friction for C1 increases continuously with sliding velocity whereas for hybrid composites (C2, C3 and C4), the COF shows a decreasing trend up to 2 m/s sliding velocity and thereafter it increases continuously for all hybrid composites (Fig. 4.19c).

4.9.4 Effect of Composition

The variation of wear rate, normalized wear rate, wear coefficient and coefficient of friction of all composites i.e. C1, C2, C3 and C4 at 1 m/s sliding velocity and 20 N normal load have been plotted in Fig. 4.20. These figures clearly show that wear rate, normalized wear rate and wear coefficient decrease with increasing vol.% of ZrB_2 in composites. While coefficient of friction increases with increase in ZrB_2 amount.

4.9.5 Surface Topography and Mechanism

Predicting wear and friction properties is not simple as large number of parameters such as environment, operating conditions and primary and secondary material properties affect the results. Though, it may not be possible to completely eliminate wear and friction under the given conditions but these can definitely be minimized by proper

material choice and by studying posttest surface conditions of the material used. Surface conditions after test can help in deciding the further action to minimize wear and friction, as well as it can also help to specify the range of parameters within which material can be used.

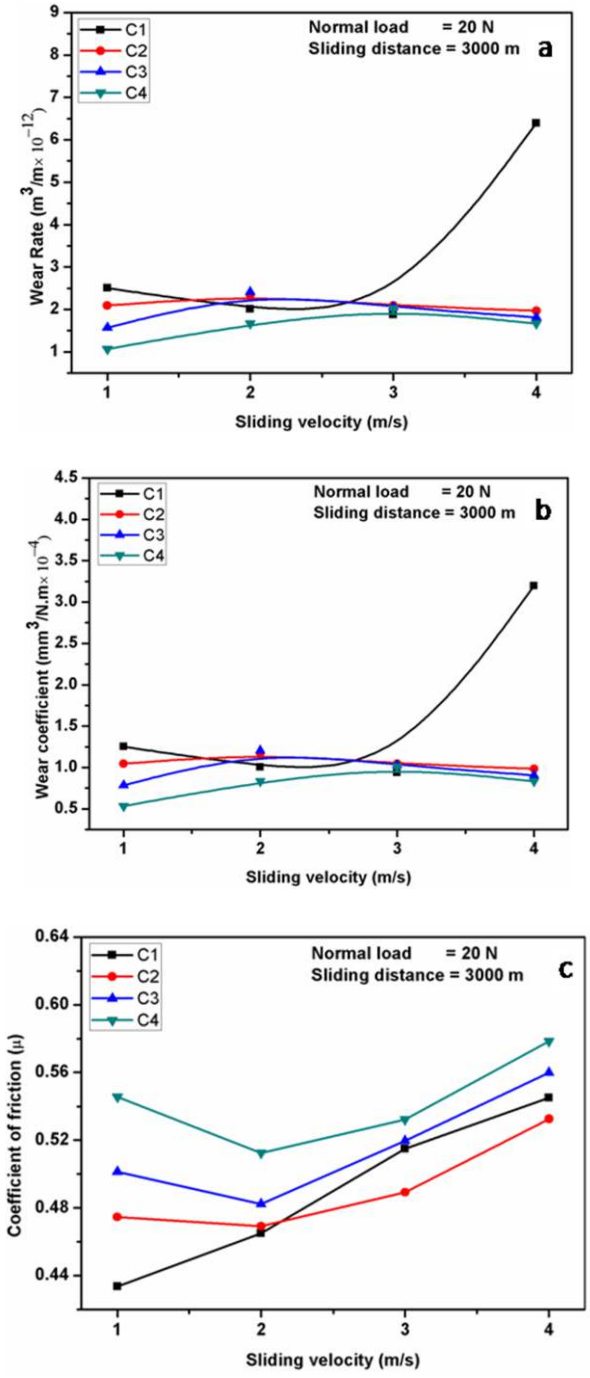

Figure 4.19 – Variation of (a) Wear rate, (b) wear coefficient, and (c) coefficient of friction with sliding speed.

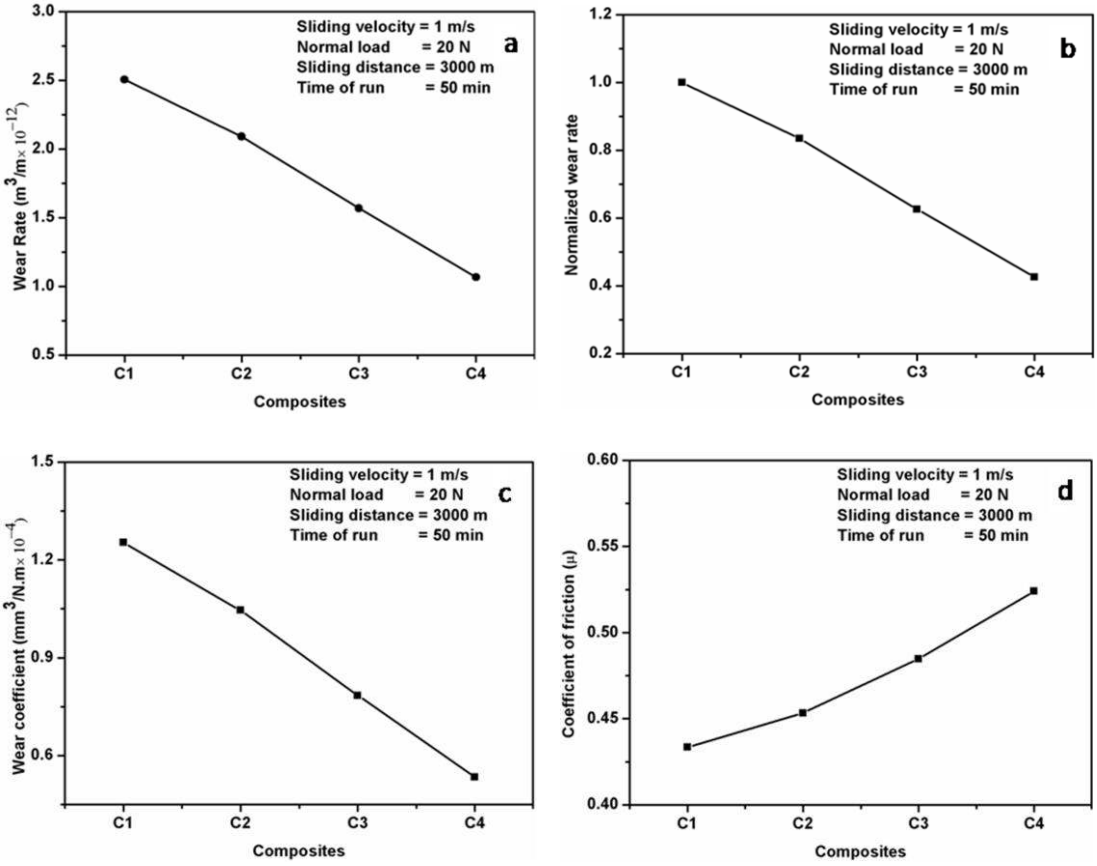

Figure 4.20 – Variation of (a) Wear rate, (b) normalized wear rate, (c) wear coefficient, and (d) coefficient of friction with different compositions.

In the present study ZrB_2 particles have been introduced in Al_3Zr/Al-Mg composites by *insitu* reaction to see their effect on the various properties of the base composite. Figure 4.17a shows cumulative wear of composites with distance which is mostly linear in nature. However, with sliding distance some fluctuations in wear rate are observed which could be due to the removal of hard particles from the surface and/or formation and breaking of oxide layer. Coefficient of friction shows fluctuations within a range of ±0.12 to ±0.25 depending on the composition (Fig. 4.17b). The fluctuations could be due to protruding of hard dispersed particles coming in contact with steel disc, and thereby increasing the coefficient of friction.

Wear rate and wear per unit vol.% reinforcement increase within the experimental load range for all compositions (Fig. 4.18a-b). Wear rate increases with same rate up to 30 N but beyond this load, wear rate increases sharply for C1 composite (without ZrB_2) which is indicative of change in wear mode from mild to severe. Once ZrB_2 is introduced in composite the sudden increase in wear rate is restricted and the wear rate remains linear up to 40 N. It indicates that transition of wear from mild to severe is delayed on inclusion of ZrB_2, however, irrespective of it wear rate continuously increases with load. Deep craters are formed and deformation of the surface takes place with increase in load as evident from 3D contours of profilometer study (Fig. 4.21a-b). The surface roughness values at 30 and 40 N load are found to be 2.23 and 4.17 μm respectively. Coefficient of friction shows completely reverse trend and it decreases with load. Though, it seems unusual but high ductility of matrix material may entrap the hard particles, or particles may be ploughed away reducing the coefficient of friction (Fig. 4.18c).

Sliding velocity is another operating parameter which affects the wear rate and wear coefficient (Fig. 4.19a-b). Composite C1 (without ZrB_2) behaves in the same manner as any other aluminium alloy or aluminium base composite in general, and both wear rate and wear coefficient decrease initially and attain a minimum value followed by a sharp increase in wear rate. But hybrid composites with ZrB_2 act differently. In these composites initially a slight increase in wear is observed and it becomes almost stabilized with a marginal decreasing trend. In wear, several phenomena take place simultaneously with increase in sliding velocity. Asperities in the matrix are either chucked out or deformed and merged within the surface, oxidation of matrix becomes pronounced with increase in temperature due to increased velocity, reinforced particles

cause decrease in wear if entrapped within the surface or may increase wear if come out and act as third body wear, and stress concentration fields are created due to large number of fine particles.

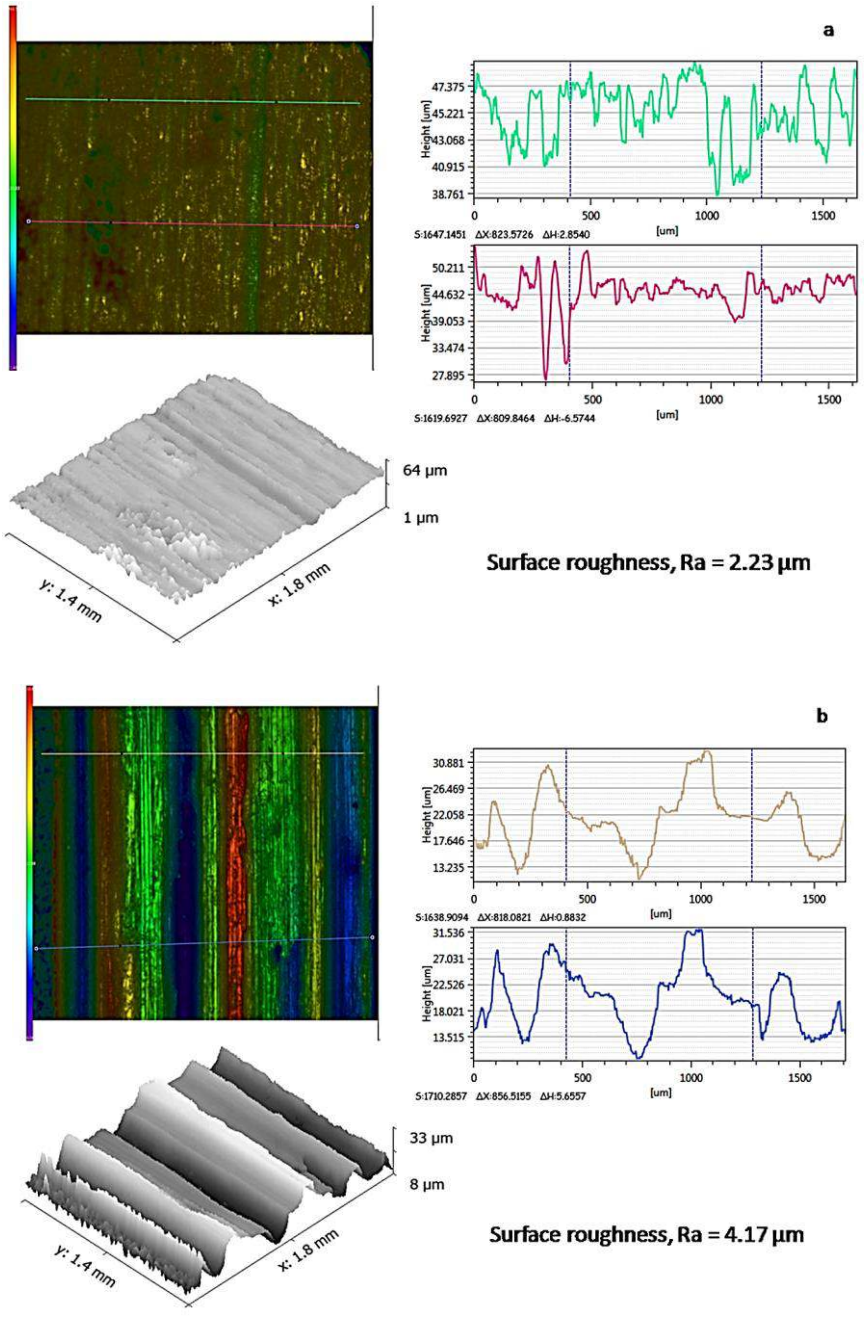

Figure 4.21 – Height analysis perpendicular to worn surface and its 3D- images for C4 composite at 1 m/s sliding velocity with different load at (a) 30 N, and (b) 40 N.

In these hybrid composites stress concentration takes place due to large number of particles that leads to crack nucleation which dominates in the initial stage of oxidation of the surface due to temperature rise, but with increase in velocity oxide particles break and rise in temperature softens the matrix phase. Al_3Zr, ZrB_2 and oxide particles instead of coming out of the surface to promote third body wear are entrapped within the surface. Though nucleation and propagation of cracks still continue giving rise to surface roughness from 0.93μm to 4.47 while sliding velocity increases from 2 to 4 m/s (Fig. 4.22a-b). But the presence of large number of hard particle dominates the wear process and restrict it to lower value. Wear coefficient also follows the same trend (Fig. 4.19a-b). On the other hand, formation of smooth oxide layer initially decreases the coefficient of friction but with increase in velocity the large number of hard particles in the contacting surface increase the coefficient of friction (Fig. 4.19c). Therefore, these *insitu* formed (Al_3Zr+ZrB_2)/Al-Mg hybrid composites could be a good candidate as wear resistant as well as friction material at high sliding velocity.

With increase in amount of ZrB_2 particles the wear rate, normalized wear rate and wear coefficient follow a decreasing trend (Fig. 4.20a-c). Again several factors contribute to this phenomenon, but as the operating parameters being the same, only stress concentration field leads to crack nucleation and propagation, and the amount of hard particles is the controlling factor for wear rate. Though, the surface gets distorted as evident from roughness contours (Fig. 4.23a-c) but level of distortion reduces as the vol.% of ZrB_2 particles increases. The hard particles dominate the overall process causing wear rate, normalized wear rate and wear coefficient to decrease and coefficient of friction to increase continuously due to the increase in number of hard particles (Fig. 4.20d).

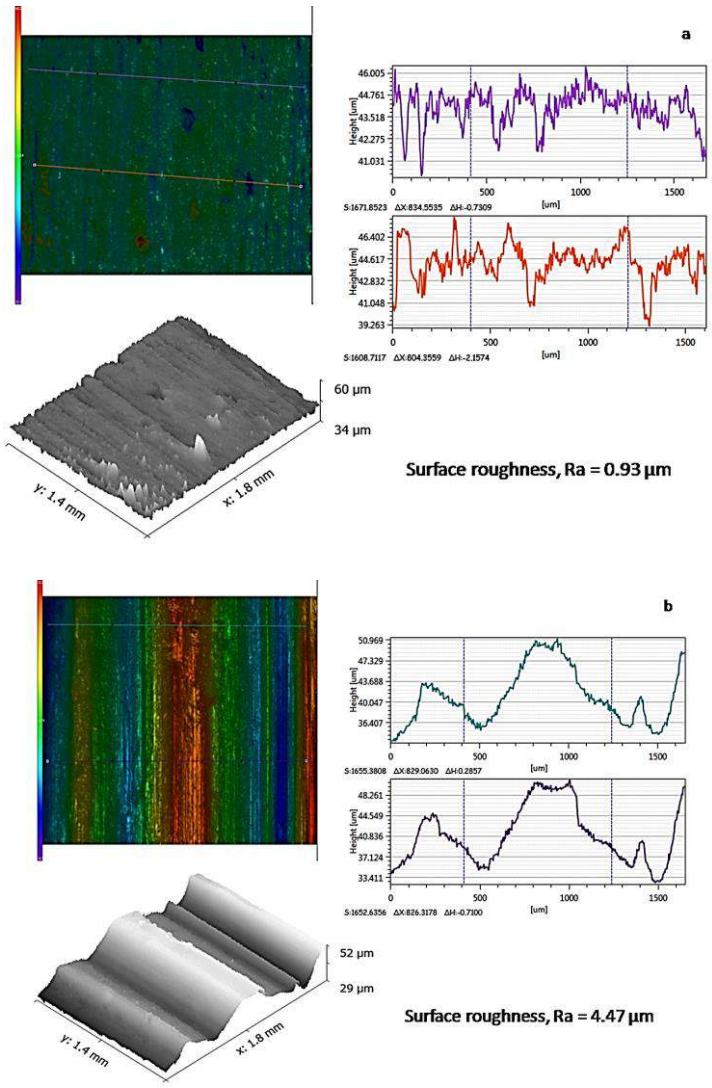

Figure 4.22 – Height analysis perpendicular to worn surface and its 3D-images for C4 composite at 20 N normal load for different sliding velocities of (a) 2 m/s, and (b) 4 m/s.

4.10 Coefficient of Linear Thermal Expansion

The coefficient of linear thermal expansion is an important parameter when materials are fabricated for the high temperature applications where dimensional tolerance becomes important. Table 4.10 shows the theoretical coefficient of linear thermal expansion and coefficient of volumetric thermal expansion for all composites. Decreasing trend in CTE values is observed as the amount of ZrB_2 particles in the Al_3Zr/Al-Mg composite increases which seems to be due to low coefficient of thermal expansion of ZrB_2 phase as compared to Al_3Zr/Al-Mg composite.

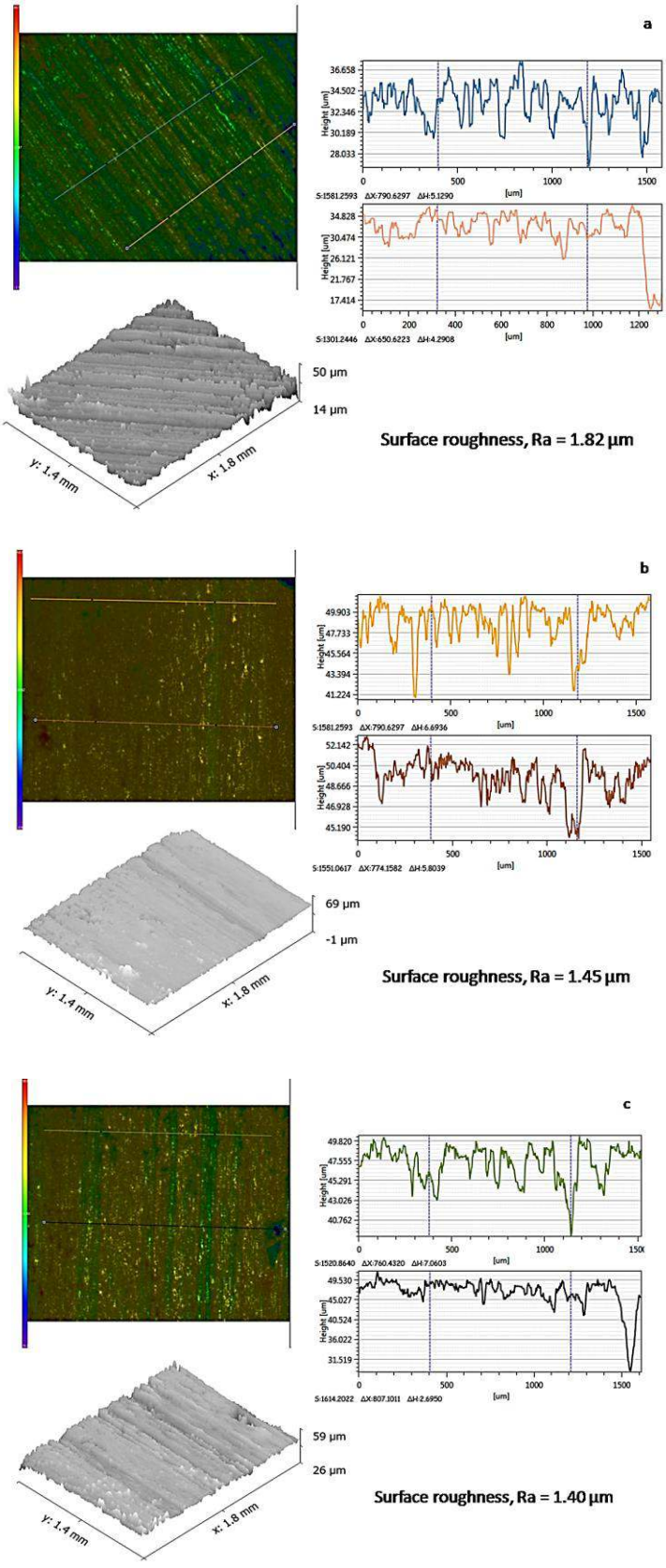

Figure 4.23 – Height analysis perpendicular to worn surface and its 3D-image at 1 m/s sliding velocity and 20 N normal loads for (a) C1, (b) C2, and (c) C3 composite.

Table 4.10 – Coefficient of linear and volumetric thermal expansion for all composites.

Composites	Theoretical Coefficient of linear thermal expansion (X 10^{-6} m/m K)	Coefficient of volumetric thermal expansion (β= 3α) (X 10^{-6} m/m K
C1	22.21	66.63
C2	21.71	65.12
C3	20.77	62.30
C4	19.90	59.70

4.11 Conclusions

On the basis of present study following conclusions are drawn:

1. The Al_3Zr/Al-Mg composite reinforced with different vol.% of ZrB_2 particles were successfully fabricated using Al-Mg alloy and inorganic salts K_2ZrF_6 & KBF_4 by direct melt reaction technique.
2. X-ray diffraction analysis (XRD) and Energy Dispersive Spectroscopy (EDS) analysis confirm the formation of ZrB_2 in the Al_3Zr/Al-Mg alloy composite.
3. *Insitu* formed ZrB_2 particles are mostly hexagonal but some rectangular shape particles are also observed. Most of the particles are within nano size range.
4. The grain size of the Al alloy matrix reduces by incorporation of ZrB_2 particles contributing to improved mechanical properties.
5. UTS and YS of the composites improve with increase in vol.% of ZrB_2 particles up to 3 vol.%, but beyond this amount UTS & YS decrease but still much higher than composite without ZrB_2. Percentage elongation also improves with addition of ZrB_2 as compared to composite without ZrB_2, but reduces with increase in ZrB_2 vol.%.

6. The composite with 3 vol.% ZrB_2 particles exhibits the maximum improvement in strength parameters UTS (150.3 MPa) and YS (116.5 MPa) which are about 40 and 80 percent higher than that of Al_3Zr/Al-Mg alloy composite.
7. Bulk hardness (BHN) of the composites improves continuously with increase in vol.% of ZrB_2 particles in Al_3Zr/Al-Mg alloy composite.
8. The strength coefficient increases with increase in ZrB_2 particles up to 3 vol.% in the Al_3Zr/Al alloy composites, whereas strain hardening decreases. However, beyond 3 vol.% ZrB_2 particles, trend of strength coefficient and strain hardening gets reversed.
9. The strengthening mechanisms affecting overall strength are dislocation, Orowan, grain-refining and solid solution in hybrid (Al_3Zr+ZrB_2)/Al-Mg composites, and among these mechanisms solid-solution and Orowan are the dominant strengthening mechanisms.
10. Experimental values of yield strength are about 5 to 8% lower than the theoretical values which could be due to the clustering of second phase particles.
11. Cumulative wear shows an increasing trend with sliding distance.
12. Wear rate with load shows that hybrid composites can be used at high load and they still remain in mild wear regime.
13. Wear rate and wear coefficient can be maintained at low values with sliding velocity on incorporation of ZrB_2 particles. Hybrid composites can be used successfully at much higher velocity and still remain in mild wear regime.
14. COF shows a fluctuating trend with sliding distance whereas it decreases with normal load.

15. COF increases with sliding velocity in Al_3Zr/Al alloy composites (without ZrB_2), but for hybrid composites, it decreases initially and beyond 2 m/s sliding velocity it increases.

16. Present investigation shows that *insitu* (Al_3Zr+ZrB_2)/Al-Mg hybrid composites could be potential candidates in applications requiring high wear resistance and high COF such as braking system.